



HAL
open science

Relationship between the base pressure and the velocity in the near-wake of an Ahmed body

Bérengère Podvin, Stéphanie Pellerin, Yann Fraigneau, Guillaume Bonnavion,
Olivier Cadot

► **To cite this version:**

Bérengère Podvin, Stéphanie Pellerin, Yann Fraigneau, Guillaume Bonnavion, Olivier Cadot. Relationship between the base pressure and the velocity in the near-wake of an Ahmed body. *Physical Review Fluids*, 2022, 7 (5), pp.054602. 10.1103/PhysRevFluids.7.054602 . hal-04193562

HAL Id: hal-04193562

<https://hal.science/hal-04193562>

Submitted on 30 Jan 2024

HAL is a multi-disciplinary open access archive for the deposit and dissemination of scientific research documents, whether they are published or not. The documents may come from teaching and research institutions in France or abroad, or from public or private research centers.

L'archive ouverte pluridisciplinaire **HAL**, est destinée au dépôt et à la diffusion de documents scientifiques de niveau recherche, publiés ou non, émanant des établissements d'enseignement et de recherche français ou étrangers, des laboratoires publics ou privés.

Relationship between the base pressure and the velocity in the near-wake of an Ahmed body

Bérengère Podvin

EM2C, CentraleSupélec, CNRS, Université Paris-Saclay, 91190 Gif/Yvette, France

Stéphanie Pellerin and Yann Fraigneau

LISN, CNRS, Université Paris-Saclay, 91190 Gif/Yvette, France

Guillaume Bonnavion

*École Nationale Supérieure de Mécanique et d'Aérotechnique,
1 Av. Clément Ader, 86360 Chasseneuil-du-Poitou, France*

Olivier Cadot

*School of Engineering, University of Liverpool, L69 3BX Brownlow Hill,
Liverpool L69 3GH, United Kingdom*



(Received 30 November 2021; accepted 20 April 2022; published 9 May 2022)

We investigate the near-wake flow of an Ahmed body which is characterized by switches between two asymmetric states that are mirrors of each other in the spanwise direction. The work focuses on the relationship between the base pressure distribution and the near-wake velocity field. Using direct numerical simulation obtained at a Reynolds number of 10^4 based on incoming velocity and body height as well as Bonnavion and Cadot's experiment [G. Bonnavion and O. Cadot, *J. Fluid Mech.* **854**, 196 (2018)], we perform proper orthogonal decomposition (POD) of the base pressure field. The signature of the switches is given by the amplitude of the most energetic, antisymmetric POD mode. However, switches are also characterized by a global base suction decrease, as well as deformations in both vertical and lateral directions, which all correspond to large-scale symmetric modes. Most of the base suction reduction is due to the two most energetic symmetric modes. Using the linear stochastic estimation technique of Podvin *et al.* [*Exp. Fluids* **59**, 58 (2018)], we show that the large scales of the near-wake velocity field can be recovered to some extent from the base pressure modes. Conversely, it is found that the dominant pressure modes and the base suction fluctuation can be well estimated from the POD velocity modes of the near-wake.

DOI: [10.1103/PhysRevFluids.7.054602](https://doi.org/10.1103/PhysRevFluids.7.054602)

I. INTRODUCTION

Bluff bodies are characterized by a large pressure drag, the reduction of which represents a significant industrial challenge in order to reduce vehicle emissions or to increase the range of electric vehicles. The present study focuses on the flat-backed Ahmed body, which represents a simplified model to study the aerodynamics of trucks, SUVs, and other flat-backed vehicles. For sufficiently large ground heights, the near-wake of the body is characterized by bistability, corresponding to asymmetric (reflection-symmetry-breaking or RSB) mirror states [1]. The variations of the pressure drag are correlated with the occurrence of intermittent switches between these two states, during

which the flow becomes briefly symmetric. It has been shown that reducing the deviation of the wake leads to drag reduction, which has motivated several control attempts [2–6].

A central question is to determine how the different velocity motions contribute to the total drag. A large number of studies have therefore focused on the description of the flow dynamics. Besides the large-scale switches between the quasistationary states, which take place on a timescale of $O(1000)$ convective time units based on the incoming flow velocity U and body height H , the flow is also characterized by three-dimensional vortex shedding, with a characteristic frequency of $0.2 U/H$, as well as deformations of the recirculation zone associated with low frequencies in the range 0.05 – $0.1 U/H$. These timescales have been identified in experiments [7,8] and confirmed by numerical simulations [9–13]. We note that all times will be expressed in convective time units based on U and H throughout the paper.

Understanding the connection between the base pressure and the near-wake flow is a key ingredient of a successful control strategy. Stochastic estimation, originally developed in a conditional average framework, can provide useful insight into this relationship. Linear stochastic estimation (LSE) was first developed by Adrian and Moin [14] to identify coherent structures in a turbulent boundary layer. Afterward its interest for control purposes was quickly made apparent [15], which spurred on a number of variants.

Several implementations of LSE are based on the combination of linear stochastic estimation with proper orthogonal decomposition (POD). Bonnet *et al.* [16] first proposed an estimate based on a low-dimensional representation of the flow. We note that a connection can be made between linear stochastic estimation and the extended POD proposed by Borée [17]. Extensions of the method include the spectral linear stochastic estimation, which has been applied to shear layers [18] as well as jets [19], and multi-time-delay stochastic estimation, which has been applied to separated flows such as a backward-facing step [20], a cavity shear layer [21], or the wake of a bluff body [22]. In [23] a new LSE-POD variant was proposed in which POD is applied to both the conditional and unconditional variables. The method was applied to a turbulent boundary layer and provided a highly resolved velocity estimate in both space and time from the combination of spatially resolved measurements with a low time resolution and time-resolved, but spatially sparse measurements.

In many studies, wall pressure measurements are used as the conditional variable to estimate the velocity field, since wall pressure sensors are nonintrusive and can easily be fitted on a body. However, it can be argued that the inverse problem is also of interest, as it allows identification of the velocity patterns that create pressure fluctuations, following boundary layer studies [24,25].

The purpose of the present paper is to investigate how the near-wake velocity field depends on the base pressure but also to determine how the fluctuations of the base pressure field are related to the dominant wake motions. To do this, we consider a direct numerical simulation of the flow behind an Ahmed body at a moderate Reynolds number $Re = 10^4$. We apply POD to extract the near-wake velocity modes, as well as the dominant base pressure structures, which we compare with the experimental results of Bonnavion and Cadot [27].

The paper is organized as follows: After describing the numerical and experimental settings, we carry out POD analysis of the base pressure and of the near-wake velocity field. Using POD-based linear stochastic estimation, we investigate the relationship between the most energetic POD pressure modes and the dominant POD velocity modes in the near-wake.

II. METHODOLOGY

A. Numerical simulation

The characteristics of the simulation have been given in [26]. The dimensions of the squareback Ahmed body are the same as in Evrard *et al.* [4]: $L = 1.124$ m, $H = 0.297$ m, $W = 0.350$ m. The ground clearance (distance from the body to the lower boundary of the domain) was taken equal to $C = 0.334H$ in the simulation. The code SUNFLUIDH, which is a finite volume solver, is used to solve the incompressible Navier-Stokes equations. The Reynolds number based on the fluid viscosity ν ,

incoming velocity U , and Ahmed body height H is 10^4 . The temporal discretization is based on a second-order backward Euler scheme, with implicit treatment of the viscous terms and explicit representation of the convective terms (Adams-Bashforth scheme). The divergence-free velocity and pressure fields are obtained from an incremental projection method [28]. We use $(512 \times 256 \times 256)$ grid points in, respectively, the longitudinal direction x , the spanwise direction y , and the vertical direction z , with a time step set to $\Delta t = 5 \times 10^{-4} H/U$ (the Courant-Friedrichs-Lewy or CFL number never exceeded 0.4). The flow was integrated over more than $500H/U$.

B. Constitution of the POD Dataset

The investigation described in this paper relies on POD analysis, which is detailed in the Appendix. We apply the method of snapshots [29] to both the fluctuating pressure c'_p and velocity fields \underline{u}' , where $c_p(t) = C_p + c'_p(t)$, $\underline{u}(t) = \underline{U} + \underline{u}'(t)$, and capital letters refer to time-averaged values. The pressure p has been translated into a pressure coefficient defined as $c_p = 2 \frac{p - p_\infty}{\rho U^2}$, where ρ is the air density, and p_∞ and U , respectively, are the free stream pressure and velocity. The velocity \underline{u} is given in U units. Due to the comparatively short extent of the time period, which is a well-known limitation of numerical simulations [30], the set of snapshots was artificially enlarged in order to enforce the statistical symmetry that would be observed if the simulation could be run for a long enough period of time. A discussion of the theoretical importance of symmetry for the application of POD can be found in [31]. Data augmentation procedures have been applied to different types of flows, such as turbulent channel flows [32,33] and Rayleigh-Bénard convection [34]. In the case of the Ahmed body, the statistical symmetry that needs to be enforced is the reflection with respect to the midvertical plane. An extended discussion of the procedure can be found in [35], which we briefly summarize here.

Statistical symmetry in the set of snapshots was enforced by adding to each snapshot extracted from the simulation the image of that snapshot through a reflection symmetry with respect to the midvertical plane. A consequence of the symmetrization procedure is that each (asymmetric) snapshot is represented as a sum of reflection-symmetric and antireflection-symmetric POD modes. Results shown in this paper were based on a set of 600 snapshots, 300 of which are directly extracted from the simulation at a sampling rate of 1 convective time unit, and 300 are virtual snapshots obtained from the original ones by application of the reflection symmetry. The time span corresponds to that used for POD in [26], that is, 300 convective time units, 200 of which correspond to the duration of a switch. As will be shown in the next sections, convergence of the POD procedure was established with respect to the number of snapshots considered for both the velocity and the pressure fields. The last 200 time units were used to test the estimation procedure for both the pressure and the velocity fields.

The normalized amplitudes of the k th modes for the pressure and velocity components will be respectively referred to as a_k^p and a_k^v . We will refer to the corresponding estimated amplitudes as a_k^{pe} and a_k^{ve} .

III. PRESSURE FIELD

POD was first applied to the fluctuating pressure field on the base of the body (see Appendix):

$$c'_p(y, z, t) = \sum_k \sqrt{\lambda_k^p} a_k^p(t) \phi_k^p(y, z). \quad (1)$$

As mentioned above, the data set was symmetrized in order to compensate for the possible lack of statistical symmetry due to the presence of very long timescales in the dataset. However, no significant difference was observed in the dominant modes corresponding to the symmetrized and the unsymmetrized (original) dataset.

POD analysis of the numerical pressure field was compared with the experimental results described in [27] for an Ahmed body having the same base aspect ratio and at a Reynolds number of

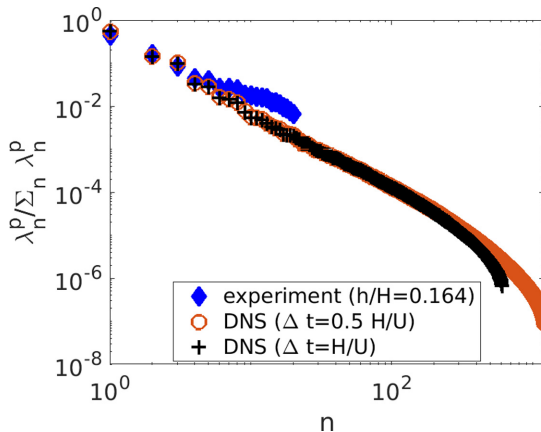


FIG. 1. POD pressure spectrum in the simulation and in the experiment [27].

$Re = 4 \times 10^5$. The same symmetrization procedure was used for the experimental data. The pressure was recovered from 21 sensors on the base of the body and then interpolated on a regular 10×10 grid to compute the spatial autocorrelation tensor from about 20 000 snapshots spanning 6000 convective time units. Since POD is a linear procedure, applying POD to the fluctuating interpolated field did not change the dimension of the data set, which is limited by the number of sensors and is therefore equal to 20. We note that the decomposition of the fluctuating pressure field yielded the same dominant modes at all ground heights investigated in the experiment for which bistability was observed, and therefore we chose to show only results corresponding to the ground height $C = 0.164H$. We note that statistical symmetry was not generally observed in the experiments, in particular, since only a limited number (about 10) of switches were observed.

Figure 1 compares the experimental and the numerical POD spectrum. The numerical POD spectra were computed for two different acquisition rates associated with time separations of $\delta U/H = 0.5$ and $\delta U/H = 1$, respectively corresponding to a total number of snapshots of 1200 and 600 snapshots. The spectra were nearly identical, with maximal differences between the eigenvalues which represented less than 1% of the total variance. The correlation coefficients between the POD amplitudes were larger than 0.95 for at least the first 20 modes, which capture more than 95% of the total variance. Convergence of the POD decomposition was therefore established. In order to make comparison between the experiment and the DNS possible, each spectrum was rescaled with the sum of the eigenvalues. A remarkably good agreement is observed, given the discrepancy in Reynolds number and spatial resolution between the simulation and the experiment. Both spectra are characterized by a similar rate of decrease $\lambda_n \sim n^{-2}$ for the largest-order modes. Based upon examination of the spectrum, we chose to focus on the first four modes, which capture 82% of the fluctuating energy in the simulation, with respective contributions of 55%, 14%, 10%, and 3% of the fluctuations.

The spatial modes are represented in Fig. 2. As is standard in the POD procedure [31], the spatial modes are normalized, i.e., $\int_{\text{base}} \phi_n(y, z) \phi_m(y, z) dy dz = \delta_{nm}$, which allows direct comparison between the numerical simulation and the experiment over the same domain. The first fluctuating POD mode $n = 1$ in Fig. 2 is antisymmetric and corresponds to the well-identified wake deviation. The evolution of POD pressure amplitudes for both the simulation (left) and the experiment (right) can be seen in Fig. 3, which represents only the original (i.e., nonsymmetrized) snapshots. The coefficients are normalized and filtered with a moving average of 10 convective time units for both experimental and numerical datasets. Evidence of switches in both the simulation and the experiment can be seen in the evolution of the first mode in the top row of Fig. 3. The total extent of the experimental data was more than 6000 convective time units, and a time window of 600 time units was selected to focus on the switching process. The times associated with the switches are indicated by a red patch

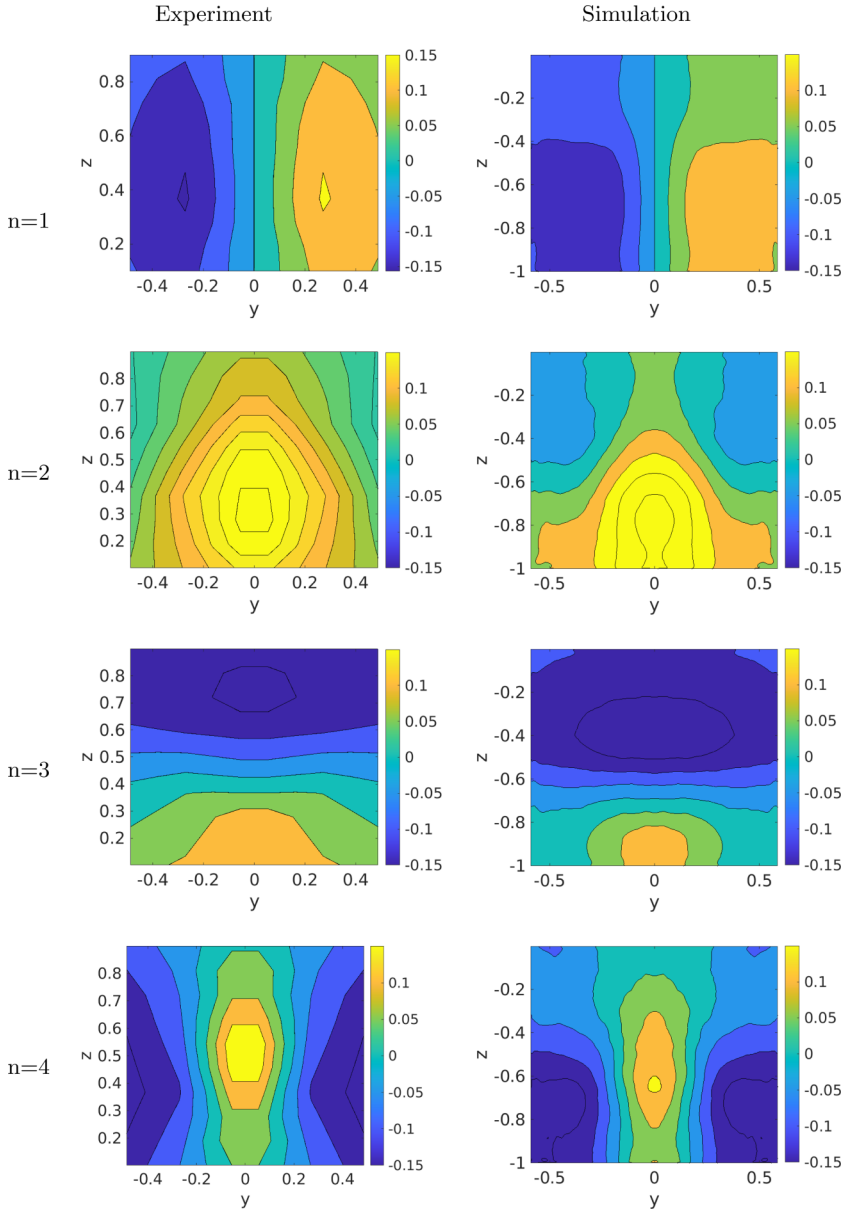


FIG. 2. POD pressure modes. Left: experiment and right: simulation.

in the figures. In both the simulation and the experiment, we can see that the normalized amplitude of mode 1 hovers near the characteristic value 1 for about 100 times units then switches sign during about 100 units, then remains negative for 100 units around the value -1 , then experiences a switch back towards the positive value. Although it seems on this particular example that switches are slightly longer in the simulation than in the experiment, evidence of longer-lasting switches was found in the experimental data. In order to provide a more robust statistical comparison, we also used joint histograms to compare the experiment and the simulation, which are presented in Fig. 4; again, only the original snapshots were used to compute the histograms.

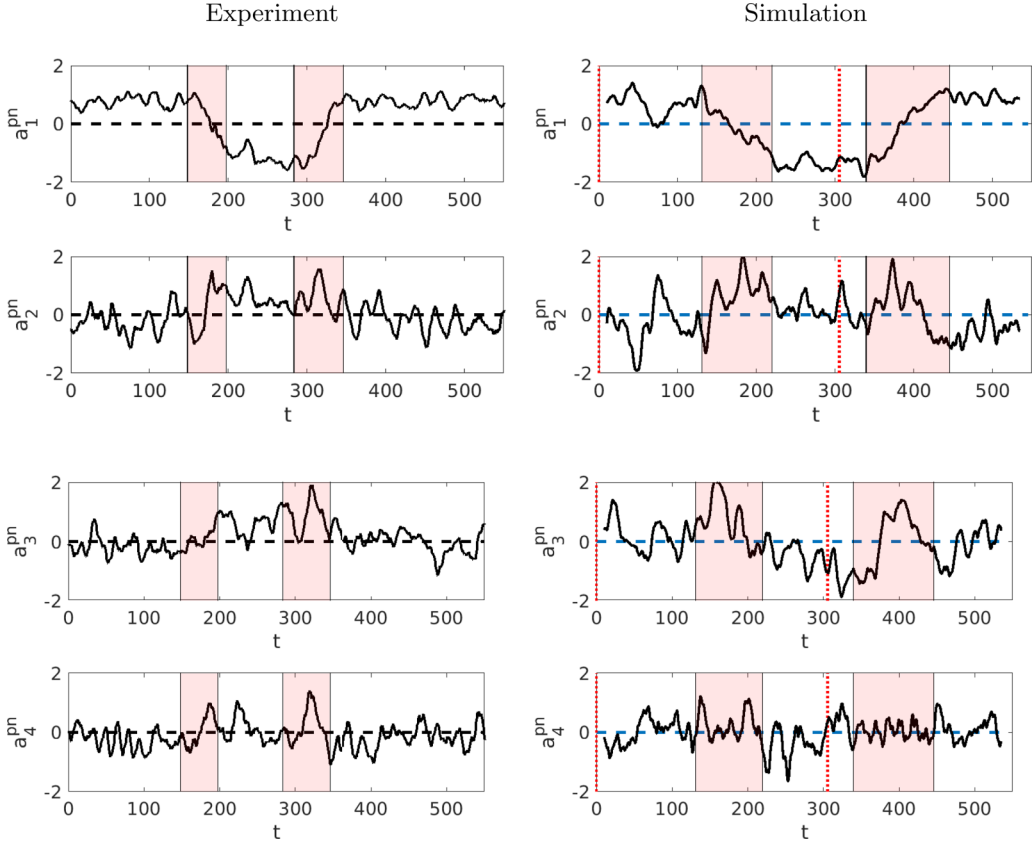


FIG. 3. Evolution of the normalized pressure POD amplitudes in the simulation (left) and the experiment (right): (top row) modes 1 and 2; (bottom row) modes 3 and 4. A moving average of ten convective time units was used.

For $n \geq 2$, the three fluctuating modes are symmetric, as can be seen in Fig. 2. The second mode $n = 2$ in Fig. 2 corresponds to a pressure variation of constant sign over the base. Its amplitude takes positive values during the switches, as can be seen in Fig. 3 and corroborated by the histograms in Fig. 4(a). This indicates that the second POD mode produces a global pressure increase during a

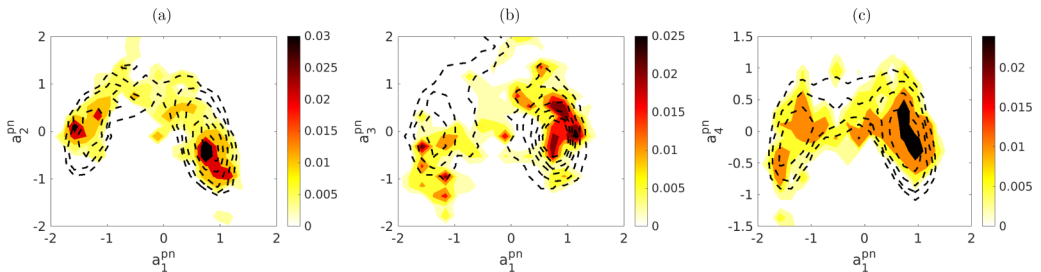


FIG. 4. Comparison of the joint histograms of the POD amplitudes a_1^{pn} and a_k^{pn} for $k = 2, 3, 4$. The color contours correspond to the numerical data. The dashed line contours correspond to the same levels for the experiment. The contour levels are the following: (a) $k = 2$: 0.003, 0.005, 0.01, 0.02, 0.03; (b) $k = 3$: 0.0025, 0.005, 0.01, 0.024; (c) $k = 4$: 0.002, 0.005, 0.01, 0.015, 0.02, 0.025. A moving average of 10 convective time units was used.

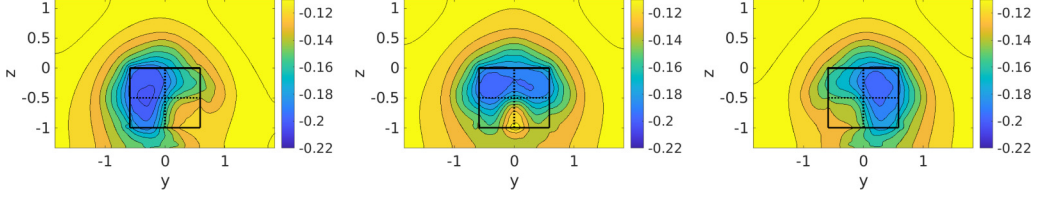


FIG. 5. Reconstruction of the mean pressure coefficient distribution at the base $c_p(y, z)$ using the symmetrized mean and the first four POD modes based on the characteristic amplitudes $a_n^{p,eq}$ and $a_n^{p,s}$: (left) quasistationary state $C_p + \sqrt{\lambda_1^p} \phi_1^p + \sum_{n=2}^4 \sqrt{\lambda_n^p} a_n^{p,eq} \phi_n^p$; (center) switch state $C_p + \sum_{n=2}^4 \sqrt{\lambda_n^p} a_n^{p,s} \phi_n^p$; (right) symmetric quasistationary state $C_p - \sqrt{\lambda_1^p} \phi_1^p + \sum_{n=2}^4 \sqrt{\lambda_n^p} a_n^{p,eq} \phi_n^p$.

switching event. The third mode $n = 3$ is characterized by strong gradients in the vertical direction. Its characteristic amplitude is weakly negative for quasistationary states, but no specific behavior could be clearly identified from the histograms in Fig. 4. We note that the first three modes are similar to the pressure modes identified by [7] for the Windsor body (see Fig. 4 from their paper) and in particular display the same symmetries. The fourth mode $n = 4$ is dominated by vertical pressure gradients at the edges of the recirculation zone. Examination of the histograms in Fig. 4(c) shows that its characteristic amplitude is negative around quasistationary states and becomes positive during the switch so that the pressure decreases on the lateral sides during the switch, which suggests that the local curvature is increased at the edges of the recirculation zone during the switch.

Characteristic amplitudes for the quasistationary state and the switching event can be defined from conditional averages based on the deviation amplitude a_1^p : $a_{n \geq 2}^{p,s} = E[a_n^p | |a_1^p| < 0.1]$ and $a_{n \geq 2}^{p,eq} = E[a_n^p | |a_1^p| > 0.9]$. In Fig. 5, a reconstruction based on these characteristic amplitudes shows the evolution of the pressure distribution as the flow goes through one switch. The pressure at the base globally increases by 5% during the switch, mostly due to the second mode, indicating a drag reduction. We note that the drag reduction level is comparable to the 7% observed in Ref. [7] during a switch.

Figure 6(a) shows the contribution of each mode to the variance of the base suction coefficient $c_b = -\frac{1}{HW} \iint_{\text{base}} c_p(y, z) dy dz$, defined as $\langle c_{bn}^2 \rangle / \langle c_b^2 \rangle$ using the classical Reynolds decomposition $c_b(t) = C_b + c_b'(t)$. The base suction, also called base drag, is the base contribution to the drag

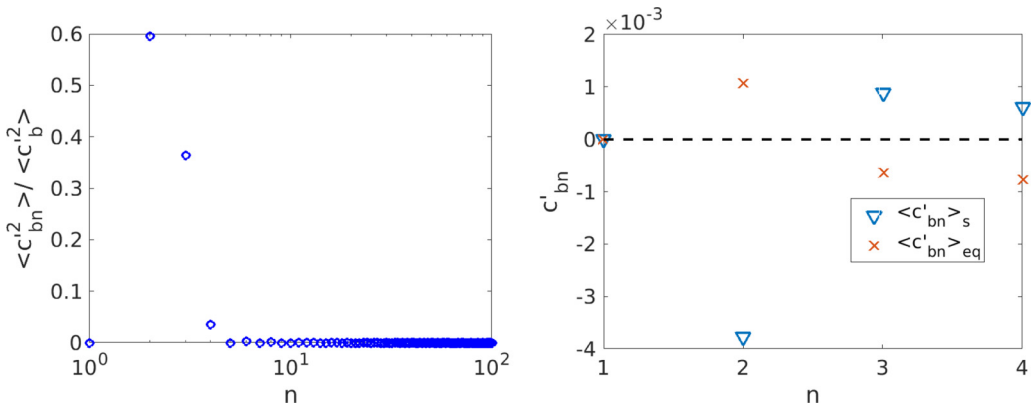


FIG. 6. (Left) Relative contribution of the POD modes to the variations of the base pressure coefficient (see text). (Right) Contribution of the modes corresponding to the characteristic states $a_n^{p,eq}$ and $a_n^{p,s}$.

TABLE I. Correlation coefficient between the velocity POD amplitude and the pressure-based estimation: (top row) for instantaneous amplitudes, and (bottom row) for amplitudes filtered with a moving average of five convective time units.

$C(a_n^v, a_n^{ve})$	$n = 1$	$n = 2$	$n = 3$	$n = 4$	$n = 5$	$n = 6$	$n = 7$	$n = 8$	$n = 9$	$n = 10$
instantaneous	0.94	0.67	0.30	0.16	0.04	0.31	0.30	0.35	0.40	0.57
averaged over $\tau = 5$	0.99	0.93	0.27	0.62	0.08	0.52	0.41	0.60	0.73	0.81

coefficient. The variance of each POD mode,

$$\langle c_{bn}^2 \rangle = \lambda_n \langle a_n^{p2} \rangle \left(\frac{1}{HW} \iint_{\text{base}} \Phi_n^p(y, z) dy dz \right)^2, \quad (2)$$

is simply related to the base suction variance by $\langle c_b^2 \rangle = \sum_n \langle c_{bn}^2 \rangle$. Only symmetric modes for which $\iint_{\text{base}} \Phi_n^p(y, z) dy dz \neq 0$ provide a nonzero contribution, and it can be seen in Fig. 6(a) that most of the base suction variations are due to the combined action of modes 2 and 3. Figure 6(b) shows the average contribution to the base suction coefficient for the characteristic events corresponding to a switch (s) or the wake in the quasistationary state (eq) identified earlier. Both contributions are evaluated with the conditional averaging $\langle c'_{bn} \rangle_{\text{eq}} = \sqrt{\lambda_n} a_n^{p,\text{eq}} \frac{1}{HW} \iint_{\text{base}} \Phi_n^p(y, z) dy dz$ and $\langle c'_{bn} \rangle_s = \sqrt{\lambda_n} a_n^{p,s} \frac{1}{HW} \iint_{\text{base}} \Phi_n^p(y, z) dy dz$. We can see that the most significant contribution is that of mode 2 during the switch, which is opposite to that of mode 3 and mode 4. The global effect of the first four POD modes is therefore to decrease the base suction during the switch.

IV. POD ANALYSIS OF THE VELOCITY FIELD IN THE NEAR-WAKE

We now consider the velocity field in the near-wake region, taken here as $-0.5H < y < 0.5H$, $-H < z < 0$, $3.8H < x < 5.5H$. The modes are computed from the autocorrelation tensor limited to the near-wake region defined above and extended to the full domain, as explained in the Appendix.

An important question is to establish whether velocity POD modes are converged. To do this we compared results for two datasets respectively consisting of 600 snapshots and 400 snapshots. The difference between the eigenvalues represented less than 0.5% of the total variance, and the Pearson correlation coefficient between the amplitudes was larger than 0.9 for the first eight POD modes and larger than 0.8 for modes 9 and 10, as can be seen in Table I.

Figure 7 shows the mean velocity field in the midheight plane restricted to the POD domain. A cross-stream section of the modes is shown at a streamwise location at $x = 4.5H$ in the middle of the recirculation zone, corresponding to the vertical line. On the velocity contours the isoline corresponding to a zero mean velocity is indicated in order to delimitate the contours of the recirculation zone. The first mode corresponds to the antisymmetric deviation mode, associated with an increased flow speed on one side and a decreased flow speed on the other side. The second mode is symmetric and was termed the switch mode, as it did not appear in an earlier study of a data set that did not include switches (see [35]). It corresponds to a velocity difference between the top and the bottom part of the recirculation zone. Modes 3, 5, and 7 are symmetric and characterized by intense fluctuations at the bottom of the recirculation zone. Modes 4, 6, and 8 are antisymmetric and are characterized by gradients in both the vertical and horizontal directions. Modes 9 and 10 are symmetric and associated with strong velocity fluctuations in the middle upper part of the recirculation zone.

To complement the description of the modes, Fig. 8 represents a view of the spatial modes extended to the entire horizontal midplane along with the power spectral density of the normalized amplitude a_n^v . The vertical black lines show the limits of the POD domain. Figure 8 shows that the first two fluctuating modes corresponding to the deviation (lateral asymmetry) and the switch (vertical asymmetry) modes extend in the far wake outside the recirculation zone. The next-order

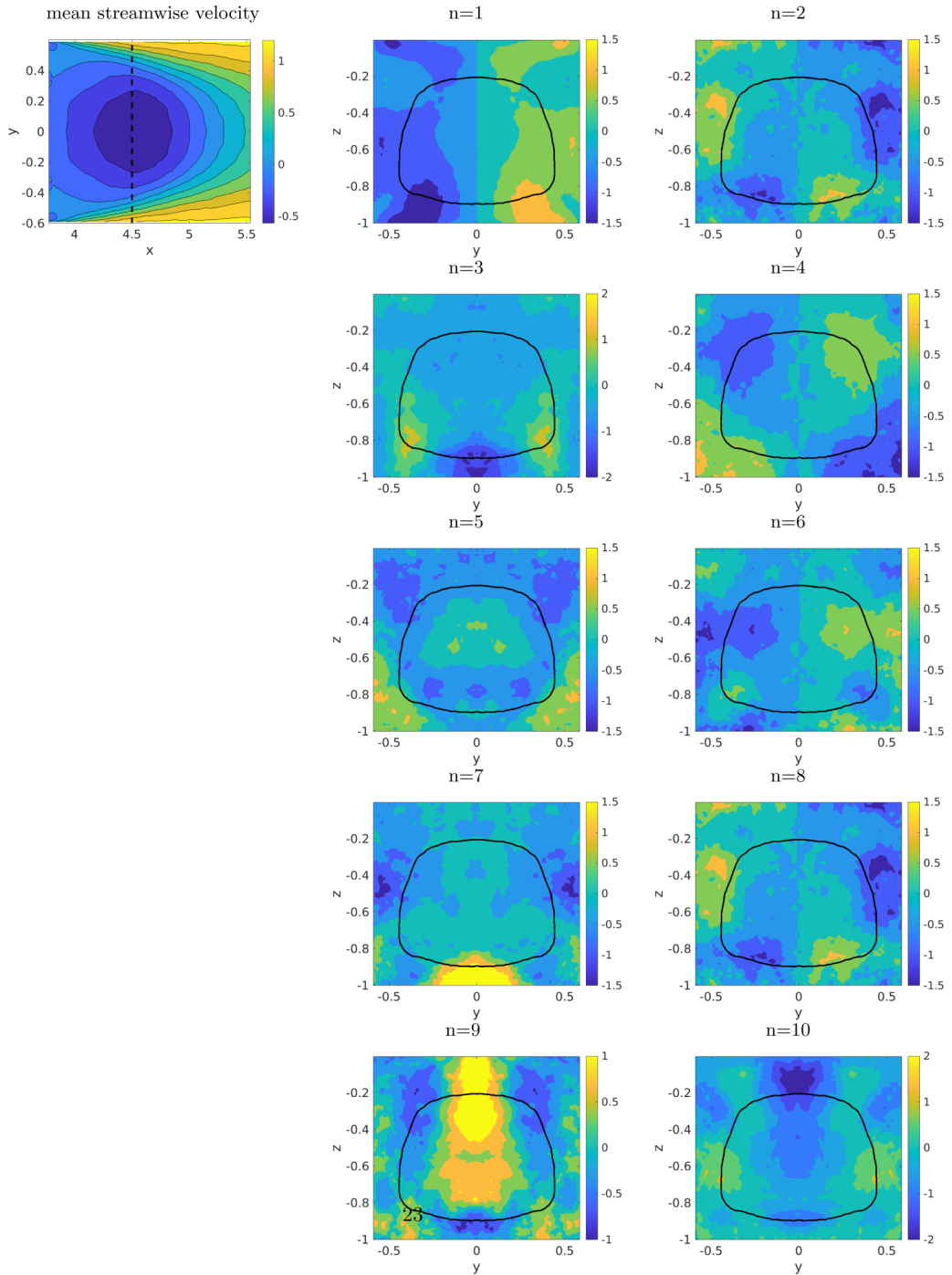


FIG. 7. Top left: mean flow in the midvertical plane. The vertical dashed line represents the cross section on which the streamwise component of the POD modes is represented in the right two columns. The black contour corresponds to a zero mean velocity.

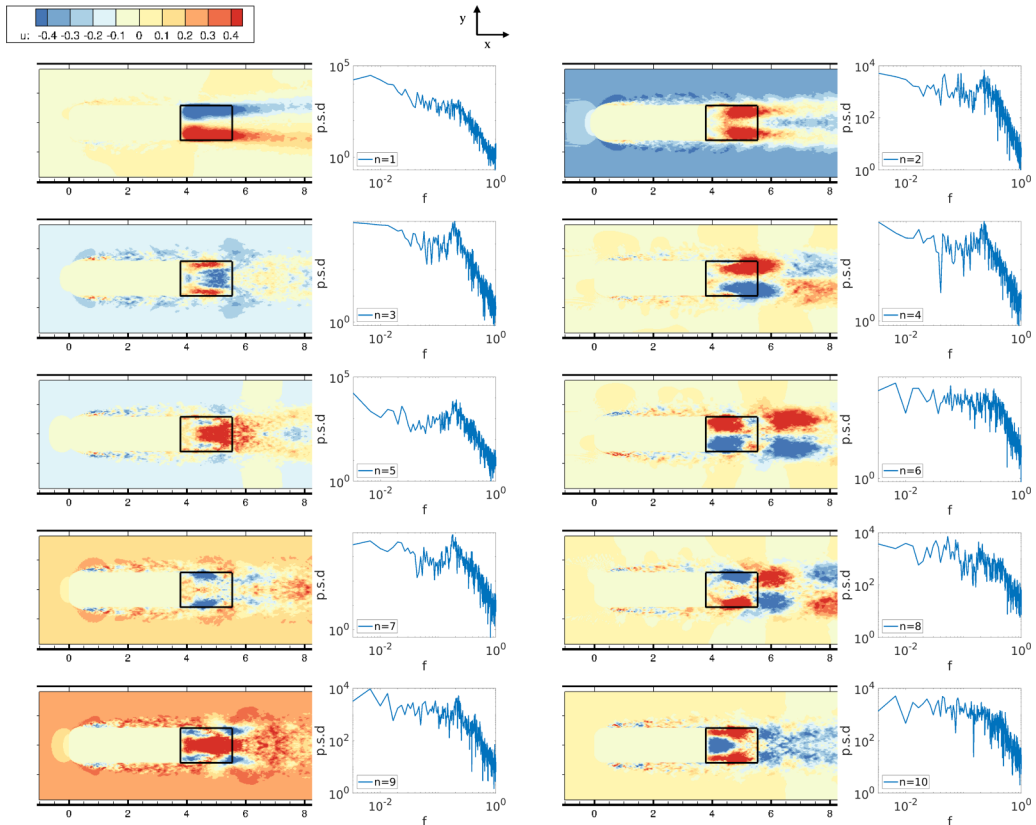


FIG. 8. Velocity modes computed over the near-wake volume (delimited with the thick black line) and extended to the full domain, viewed in a horizontal plane at midheight.

modes are a mixture of vortex shedding dynamics characterized by a peak at the frequency of $fH/U \sim 0.2$, as can be seen particularly for modes 4, 6, and 8, which correspond to lateral vortex shedding, while the vertical vortex shedding motions associated with modes 3, 5, and 7 cannot be seen on the midplane view (see [26] for a fuller discussion). These modes are characterized by strong shear layers on the outside of the recirculation zone and are associated with intense fluctuations in the far wake.

Results are consistent with those obtained with a decomposition applied to the full numerical domain ([35,26]). The hierarchy of the modes is generally similar; however, some variations can be observed in their relative energy content. The relative importance of the switch mode to the deviation mode λ_2/λ_1 remains about the same (26% versus 21% in the near-wake), but the relative importance of the vortex shedding modes compared to the energy of the deviation mode λ_1 is decreased by almost a factor of 2, as it changes from 62% in the full domain to only 34% in the far wake. In contrast, the relative content of the next-order modes (modes 7–10) decreases by less than 30%, from 36% to 23%.

V. POD-BASED LINEAR STOCHASTIC ESTIMATION

A. Method

In this section we describe the principle of the POD-LSE method [23]. We suppose that two different quantities \underline{h} and \underline{q} can be extracted simultaneously from a set of N snapshots. The quantities

may have different dimensions (in particular, they may be scalars) and can be defined on the same or different parts of the domain. Independent POD decomposition of each set of snapshots yields

$$\underline{q}(\underline{x}, t_i) = \sum_{n=1}^N a_n^q(t_i) \underline{\phi}_n^q(\underline{x}), \quad \underline{h}(\underline{x}, t_i) = \sum_{n=1}^N a_n^h(t_i) \underline{\phi}_n^h(\underline{x}). \quad (3)$$

The idea is then to use POD to estimate one quantity (for instance \underline{h}) based on measurements of the other (for instance, \underline{q}). For each time t_i , $i = 1, \dots, N$, the N coefficients $a_n^h(t_i)$ can be obtained from the mapping,

$$a_n^h(t_i) = M_{nk}^{hq} a_k^q(t_i), \quad (4)$$

where

$$M^{hq} = A^h (A^q)^T.$$

A^h and A^q are respectively the matrices consisting of rows of coefficients $a_n^h(t_i)$ and $a_n^q(t_i)$:

$$A^h = \begin{bmatrix} a_1^h(t_1) & a_1^h(t_2) & \dots & a_1^h(t_N) \\ a_2^h(t_1) & a_2^h(t_2) & \dots & a_2^h(t_N) \\ \dots & \dots & \dots & \dots \\ a_N^h(t_1) & a_N^h(t_2) & \dots & a_N^h(t_N) \end{bmatrix}.$$

The expression is exact for the snapshots of the database t_i if the full N th-order matrix is used. However, if the matrix is truncated, one can still obtain an estimate at any time t of the first $N_h \leq N$ POD amplitudes based on a subset of $N_q \leq N$ POD amplitudes using

$$a_n^{he}(t) = \tilde{M}_{nk}^{hq} a_k^q(t), \quad (5)$$

where \tilde{M} is a submatrix of M containing the N_h rows and N_q columns. A high value of the matrix entry \tilde{M}_{nk}^{hq} indicates that the k th mode of q has a strong influence on the n th mode of \underline{h} . The final step of the estimation method is to normalize the estimate with its standard deviation on the set of POD snapshots:

$$a_k^{he}(t) \rightarrow \frac{\sqrt{N}}{\sqrt{\sum_{i=1}^N |a_k^{he}(t_i)|^2}} a_k^{he}(t).$$

In the paper the method is applied to the base pressure p and the velocity field \underline{u} in the near-wake. The aim is to determine whether a linear relationship exists between the base pressure modes and the velocity modes. The estimation matrix is determined from the snapshots constituting the set used to compute the POD modes, which spanned 300 time units of the simulation. It is then tested to reconstruct the velocity (resp. pressure) field from pressure (resp. velocity) measurements corresponding to the next 200 time units. Since the turbulent flow is characterized by apparently chaotic dynamics, the snapshots constituting the test database can be assumed to be decorrelated from those used to compute the POD modes.

B. Determining the velocity field from the pressure

We first investigate the dependence of the velocity field on the base pressure in the near-wake. We then examine the largest velocity modes, focusing on the large scales with a moving time average of five convective time units, which corresponds to the vortex shedding period. Figures 9 and 10 compare the evolution of the exact velocity mode amplitude with its pressure-based estimation using

$$a_n^{ve}(t) = \tilde{M}_{nk}^{vp} a_k^p(t). \quad (6)$$

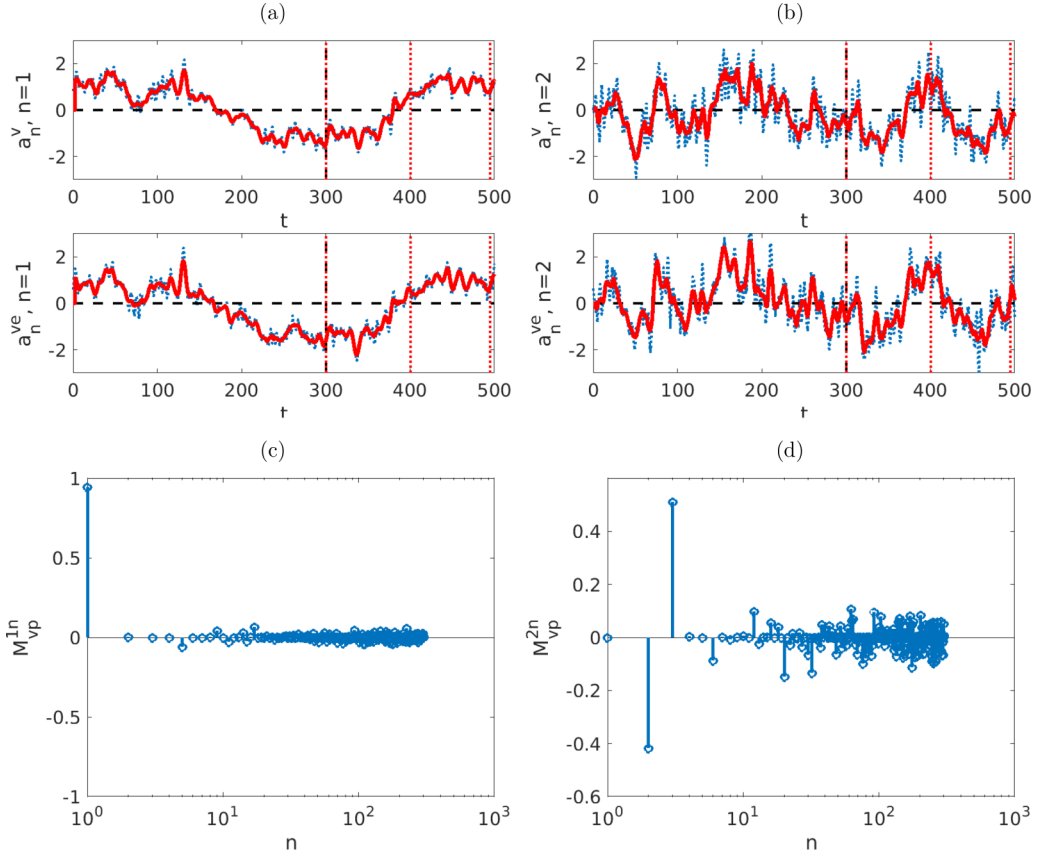


FIG. 9. (a), (b) Velocity mode contribution to first POD mode M_{1n}^{vp} (a) and second POD mode M_{2n}^{vp} (b). (c), (d) Velocity POD amplitudes for the first (c) and second mode (d). The top row corresponds to the exact coefficient a_n^v . The bottom row corresponds to the estimated coefficient $a_n^{v,e}$. The dotted line represents the instantaneous signal, and the red thick line to the signal filtered with a moving average of five time units. The vertical dashed line corresponds to the limit of the POD snapshot acquisition. The three red dotted lines correspond to the times selected for reconstruction in Fig. 11.

We can see that the first two POD velocity modes, i.e., the deviation and the switch mode, are well estimated from the pressure coefficients. Figure 9 shows that the first fluctuating velocity and pressure modes are perfectly correlated, while the switch mode can be estimated from the difference from the second and third POD pressure modes. Table I presents the correlation coefficient between the velocity POD amplitudes and the pressure-based estimates. We can see that modes 8, 9, and 10 are very well correlated with the pressure estimation, particularly if a moving average of length 5 time units is applied in order to remove the high frequencies associated with vortex shedding. Figure 10 shows that the POD amplitude of modes 9 and 10 is well estimated. Comparison of Figs. 2 and 7 suggests that this could be due to the good spatial correlation of modes 9 and 10 with the most energetic pressure modes.

Figure 11 compares instantaneous fields with their projection on the ten most energetic velocity modes and estimation for three different times (indicated by the vertical lines in Figs. 9 and 10) corresponding to a quasistationary asymmetric state, a nearly symmetric state, and the opposite asymmetric state. We can see that the large scales of the near-wake flow are very well estimated from the pressure base measurements. However, the vortex shedding modes are not very well reconstructed from the pressure modes, which suggests that these modes have a limited influence on

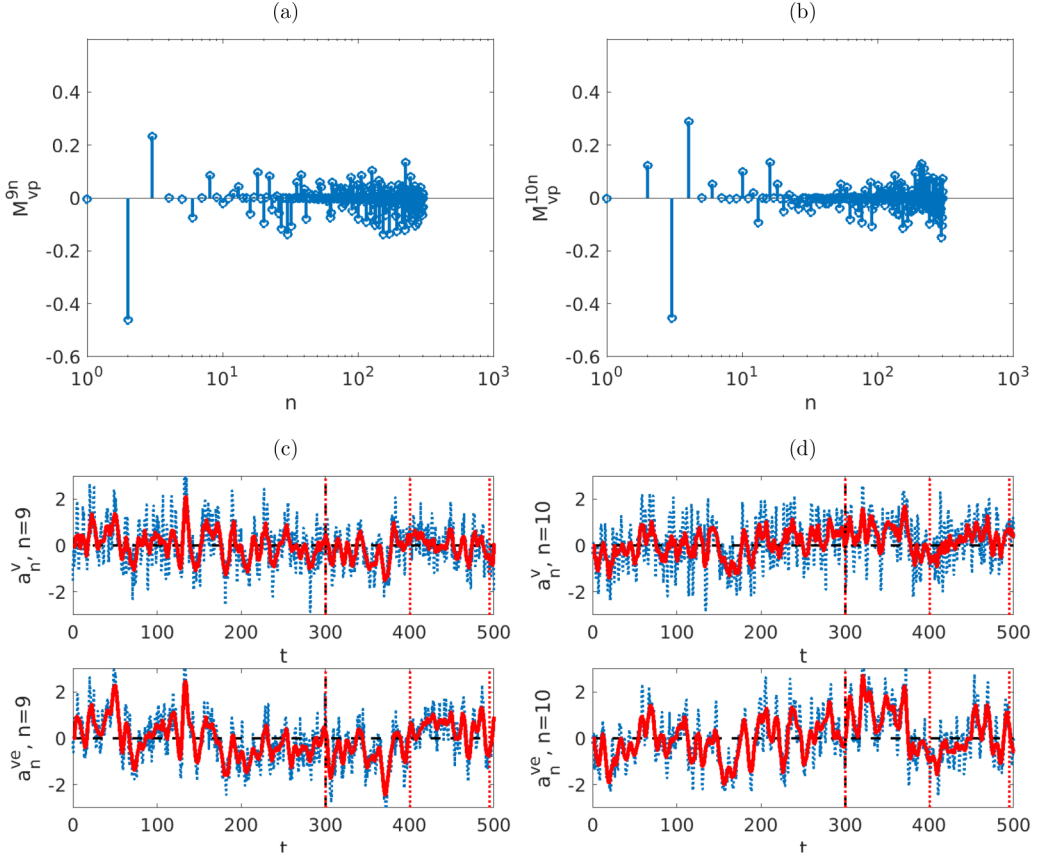


FIG. 10. (a), (b) Influence coefficients M_{9n}^{vp} (a) and M_{10n}^{vp} (b). (c), (d) Velocity POD amplitudes for the ninth (c) and tenth mode (d). Legend as in Fig. 9.

the dynamics of the recirculation zone. This is supported by examination of Fig. 7, which suggests that the fluctuations associated with modes are strongest outside the recirculation zone.

C. Reconstructing the pressure from the near-wake field

Figure 12 compares the real pressure POD amplitudes (extracted from the simulation) a_n^p with their estimation a_n^{pe} , based on ten velocity modes using Eq. (5):

$$a_n^{pe}(t) = \tilde{M}_{nk}^{pv} a_k^v(t). \quad (7)$$

A good agreement is observed, with a nearly perfect correlation for the first fluctuating mode corresponding to the deviation amplitude, and high correlation coefficients particularly for the second and the third modes, as can be seen in Table II. We note that due to antisymmetry, the dominant deviation pressure mode does not contribute to the base suction fluctuation $c'_b(t)$, the variations of which are due to symmetric modes only.

Figure 13 shows that the second pressure mode is mostly determined by velocity modes 2, 3, and 9, while the third pressure mode was mostly associated with modes 2 and 10. This is not entirely surprising, since the imprint of the pressure modes on velocity modes 9 and 10 was found to be large. Since the pressure modes 2 and 3 contribute most to the pressure coefficient (Fig. 6), we constructed

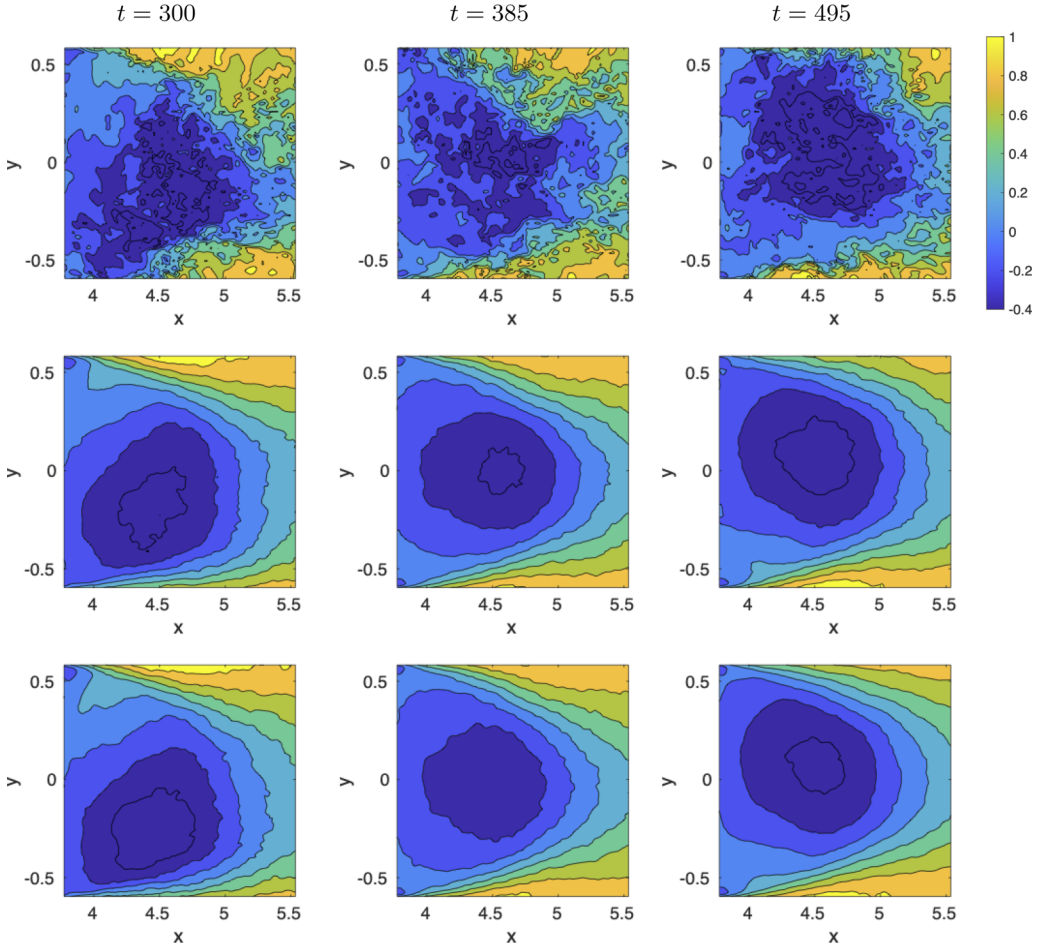


FIG. 11. Streamwise velocity field at three instants $t = 300, 385, 495$ materialized by the vertical dotted lines in Figs. 9 and 10: (top row) DNS field; (middle row) field projected on the first ten POD velocity modes; (bottom row) field estimated from the first ten POD pressure modes.

an estimation of the pressure coefficient from the second and third POD pressure modes,

$$c_b^{pe} = - \sum_{n=2}^3 \lambda_n^{p,1/2} a_n^{pe} \frac{1}{HW} \iint_{\text{base}} \phi_n^p dydz, \quad (8)$$

TABLE II. Correlation coefficient between the pressure POD amplitude and the velocity-based estimation: (top row) for instantaneous amplitudes, and (bottom row) for amplitudes filtered with a moving average of five convective time units.

$C(a_n^p, a_n^{pe})$	$n = 1$	$n = 2$	$n = 3$	$n = 4$	$n = 5$
instantaneous	0.94	0.67	0.82	0.31	0.37
averaged over $\tau = 5$	0.99	0.86	0.91	0.44	0.80

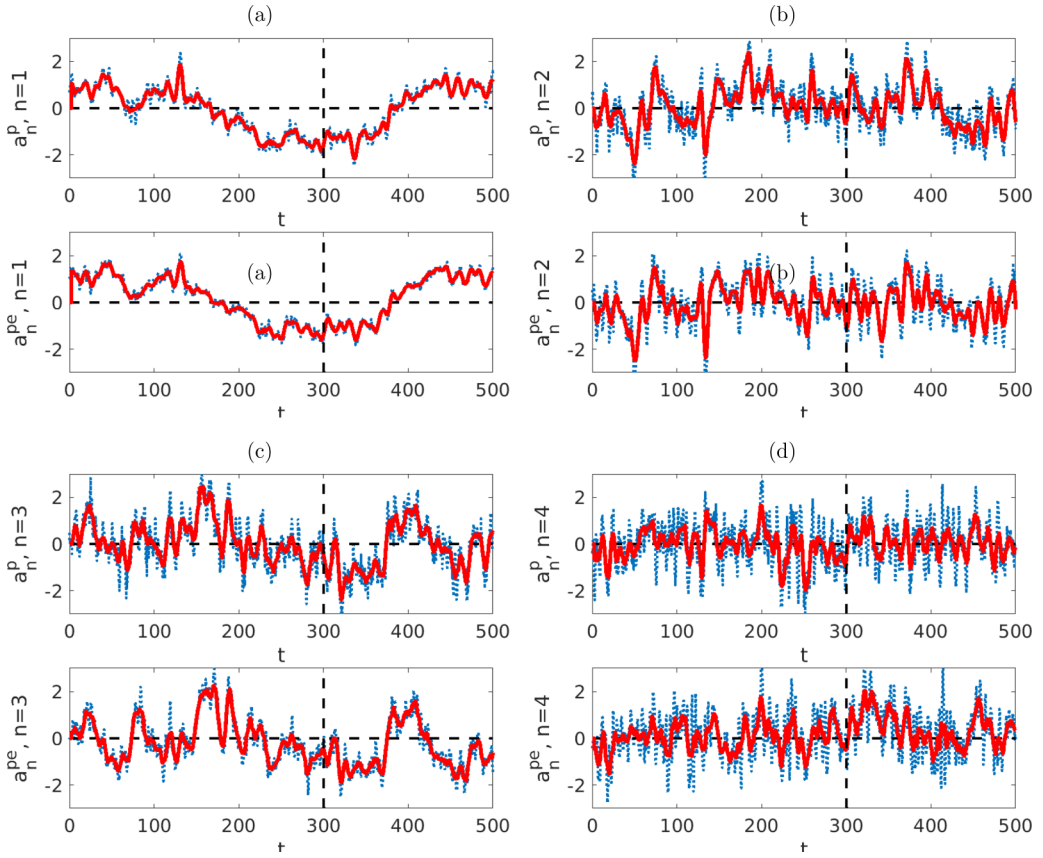


FIG. 12. Base pressure POD coefficients estimated from the near-wake velocity field. The top row of each subfigure corresponds to the exact coefficient a_n^p . The bottom row corresponds to the estimated coefficient $a_n^{p,e}$. The dotted line represents the instantaneous coefficient and the red thick line to it being filtered with a moving average of five time units. The dashed vertical line corresponds to the limit of the POD snapshot acquisition. (a) $n = 1$, (b) $n = 2$, (c) $n = 3$, and (d) $n = 4$.

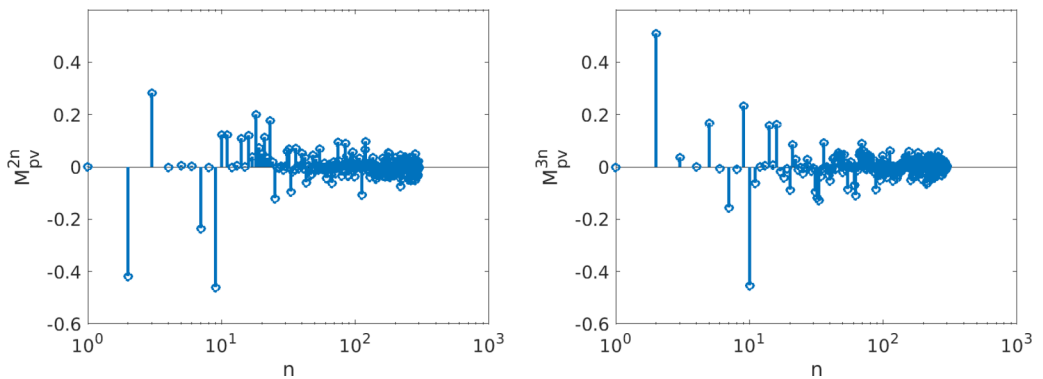


FIG. 13. Pressure contribution to second velocity mode M_{2n}^{pv} (a) and third velocity mode M_{3n}^{pv} (b).

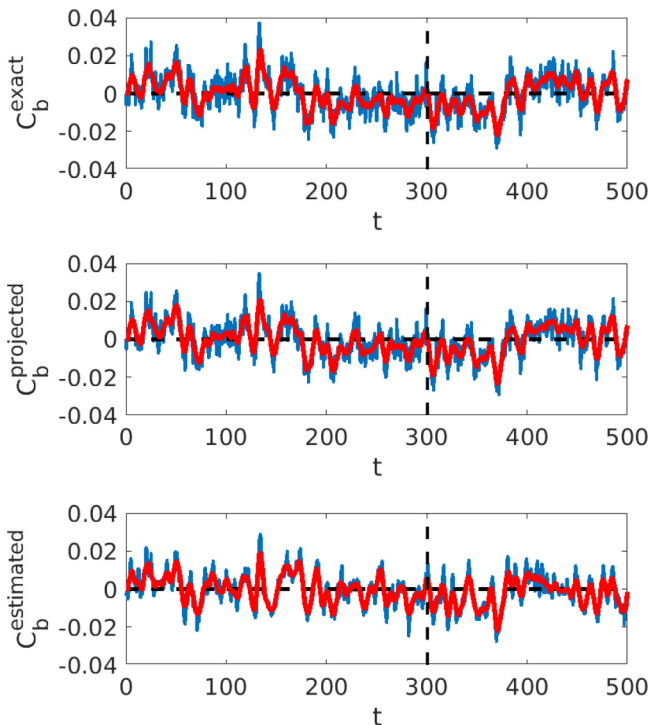


FIG. 14. Base drag coefficient: (top) DNS, (middle) reconstruction based on pressure modes 2 and 3, and (bottom) estimation based on POD velocity modes. The dashed vertical line corresponds to the limit of the POD snapshot acquisition.

which we compared with the equivalent projection,

$$c_b^{\text{proj}} = - \sum_{n=2}^3 \lambda_n^{p,1/2} a_n^p \frac{1}{HW} \iint_{\text{base}} \phi_n^p dydz. \quad (9)$$

Results are shown in Fig. 14. As expected, the agreement between the full pressure coefficient and its projection is excellent. A very good agreement is obtained for the estimation. The correlation coefficient between the full drag and estimated one is 0.7 and increases to 0.8 with a moving average of length five convective units.

VI. CONCLUSION

We have investigated how the wake dynamics in the flow around an Ahmed body can be described using POD analysis of the base pressure. Decomposition of the pressure field shows that the switch is characterized by the following modifications of the pressure distribution: (i) a global increase over the body base, (ii) a gradient in the vertical direction, and (iii) a symmetric lateral gradient within the recirculation zone corresponding to a pressure increase along the midvertical plane and decrease in the outer recirculation zone. These features were identified in both the numerical simulation and in experimental results. The signature of the pressure modes could clearly be identified in the evolution of the dominant POD velocity modes. The fluctuating velocity field, in particular the most energetic deviation and switch modes, was well recovered from pressure measurements. Conversely, variations of the pressure drag coefficient, which are essentially determined by the largest two symmetric pressure modes, could be well recovered from the near-wake velocity field.

ACKNOWLEDGMENT

We thank the anonymous referees for their comments which have helped us improve the manuscript.

APPENDIX: POD

The main tool of analysis used in this paper is proper orthogonal decomposition (POD) [36]. We consider a spatiotemporal vector field $\tilde{q}(\underline{x}, t)$ defined on a spatial domain D . $\tilde{q}(\underline{x}, t)$ will refer either to the pressure field p or the velocity field \underline{u} . The fluctuating part of the field \underline{q} (with respect to its temporal mean) can be expressed as a superposition of spatial modes,

$$\underline{q}(\underline{x}, t) = \sum_k \tilde{a}_k(t) \underline{\phi}_k(\underline{x}), \quad (\text{A1})$$

where the spatial modes $\underline{\phi}_k$ are orthogonal (and can be made orthonormal), i.e.,

$$\int_D \underline{\phi}_k(\underline{x}) \cdot \underline{\phi}_m(\underline{x}) d\underline{x} = \delta_{km},$$

and the amplitudes a_k are uncorrelated. The modes can be ordered by decreasing energy $\lambda_1 \geq \lambda_2 \geq \dots \geq \lambda_k = \langle \tilde{a}_k \tilde{a}_k \rangle$, where $\langle \cdot \rangle$ represents a time average.

The amplitudes \tilde{a}_k can be obtained from the knowledge of the spatial modes by projection of the vector field \underline{q} onto the spatial modes:

$$\tilde{a}_k(t) = \int_{\Omega} \underline{u}(\underline{x}, t) \cdot \underline{\phi}_k(\underline{x}) d\underline{x}. \quad (\text{A2})$$

The modes ϕ_k and the values λ_k can be obtained from the eigenproblem (direct method)

$$\int_D C(\underline{x}, \underline{x}') \cdot \underline{\phi}_m^q(\underline{x}') d\underline{x}' = \lambda_k \underline{\phi}_k(\underline{x}), \quad (\text{A3})$$

where C is the spatial autocorrelation tensor

$$C(\underline{x}, \underline{x}') = \langle \underline{q}(\underline{x}, t) \underline{q}(\underline{x}', t') \rangle.$$

Alternatively, if the number of snapshots N used to compute C is smaller than the spatial dimension of the problem, one can obtain the modes through the method of snapshots where

$$\bar{C}_{ij} \cdot A_{jk} = \lambda_k A_{ik}, \quad (\text{A4})$$

where $A_{jk} = a_k(t_j)$, and \bar{C} is the temporal autocorrelation matrix,

$$\bar{C}_{ij} = \frac{1}{N} \int_D \underline{q}(\underline{x}, t_i) \cdot \underline{q}(\underline{x}, t_j) d\underline{x}.$$

We note that spatial modes obtained for quantity \underline{q} on a domain D can be extended to another quantity \underline{q}' (which can be, for instance, the same quantity \underline{q} on a domain D') [17] using

$$\phi_n^{q'}(\underline{x}, t) = \sum_{k=1}^N a_n^q(t_k) \underline{q}'(\underline{x}, t_k). \quad (\text{A5})$$

In this paper we consider pressure and velocity decompositions and index the corresponding amplitudes as a_k^p and a_k^v , respectively. In the paper we will consider normalized amplitudes defined as $a_k = \tilde{a}_k / \sqrt{\lambda_k}$.

- [1] M. Grandemange, M. Gohlke, and O. Cadot, Turbulent wake past a three-dimensional blunt body. Part 1. Global modes and bi-stability, *J. Fluid Mech.* **722**, 51 (2013).
- [2] D. Barros, T. Ruiz, J. Borée, and B. Noack, Control of three-dimensional blunt body wake using low and high frequency pulsed jets, *Int. J. Flow Control* **6**, 61 (2014).
- [3] R. Li, D. Barros, J. Borée, O. Cadot, B. Noack, and L. Cordier, Feedback control of bimodal wake dynamics, *Exp. Fluid* **51**, 158 (2016).
- [4] A. Evrard, O. Cadot, V. Herbert, D. Ricot, R. Vigneron, and J. Delery, Fluid force and symmetry breaking modes of a 3D bluff body with a base cavity, *J. Fluids Struct.* **61**, 99 (2016).
- [5] R. Brackston, J. G. D. L. Cruz, A. Wynn, G. Rigas, and J. Morrison, Stochastic modelling and feedback control of bistability in a turbulent bluff body wake, *J. Fluid Mech.* **802**, 726 (2016).
- [6] B. Plumejeau, S. Delpart, L. Keirsbulck, M. Lippert, and W. Abassi, Ultra-local model-based control of the square-back Ahmed body wake flow, *Phys. Fluids* **31**, 085103 (2019).
- [7] G. Pavia, M. Passmore, and C. Sardu, Evolution of the bi-stable wake of a square-back automotive shape, *Exp. Fluids* **59**, 2742 (2018).
- [8] A. Perry, G. Pavia, and M. Passmore, Influence of short rear end tapers on the wake of a simplified square-back vehicle: Wake topology and rear drag, *Exp. Fluids* **57**, 169 (2016).
- [9] J. Lucas, O. Cadot, V. Herbert, S. Parpais, and J. Délerly, A numerical investigation of the asymmetric wake mode of a squareback Ahmed body – Effect of a base cavity, *J. Fluid Mech.* **831**, 675 (2017).
- [10] O. Evsafyeva, A. Morgans, and L. D. Longa, Simulation and feedback control of the Ahmed body flow exhibiting symmetry breaking behaviour, *J. Fluid Mech.* **817**, R2 (2017).
- [11] A. Rao, G. Minelli, B. Basara, and S. Krajnovic, On the two flow states in the wake of a hatchback Ahmed body, *J. Wind Eng. Ind. Aerodyn.* **173**, 262 (2018).
- [12] L. Dalla Longa, O. Evstafyeva, and A. S. Morgans, Simulations of the bi-modal wake past three-dimensional blunt bluff bodies, *J. Fluid Mech.* **866**, 791 (2019).
- [13] Y. Fan, X. Chao, S. Chu, Z. Yang, and O. Cadot, Experimental and numerical analysis of the bi-stable turbulent wake of a rectangular flat-backed bluff body, *Phys. Fluids* **32**, 105111 (2020).
- [14] R. Adrian and P. Moin, Stochastic estimation of organized turbulent structure: Homogeneous shear flow, *J. Fluid Mech.* **190**, 531 (1988).
- [15] J. Taylor and M. Glauser, Towards practical flow sensing and control via POD and LSE-based low-dimensional tools, in *ASME 2002 Fluids Engineering Division Summer Meeting, Montreal, Quebec, 14–18 July 2002* (ASME, New York, 2002).
- [16] J. Bonnet, D. Cole, J. Delville, M. Glauser, and L. Ukeiley, Stochastic estimation and proper orthogonal decomposition: Complementary techniques for identifying structure, *Exp. Fluids* **17**, 307 (1994).
- [17] J. Boree, Extended proper orthogonal decomposition: A tool to analyse correlated events in turbulent flows, *Exp. Fluids* **35**, 188 (2003).
- [18] J. Citriniti and W. George, Reconstruction of the global velocity field in the axisymmetric mixing layer utilizing the proper orthogonal decomposition, *J. Fluid Mech.* **418**, 137 (2000).
- [19] C. Tinney, F. Coiffet, J. Delville, A. Hall, P. Jordan, and M. Glauser, On spectral linear stochastic estimation, *Exp. Fluids* **41**, 763 (2007).
- [20] L. Hudy and A. Naguib, Stochastic estimation of a separated-flow field using wall-pressure-array measurements, *Phys. Fluids* **19**, 024103 (2007).
- [21] D. Lasagna, M. Orazi, and G. Iuso, Multi-time delay, multi-point linear stochastic estimation of a cavity shear layer velocity from wall-pressure measurements, *Phys. Fluids* **25**, 017101 (2013).
- [22] V. Durgesh and J. Naughton, Multi-time delay, multi-point linear stochastic estimation of a cavity shear layer velocity from wall-pressure measurements, *Exp. Fluids* **49**, 571 (2010).
- [23] B. Podvin, S. Ngumatsia, J. Foucaut, C. Cuvier, and Y. Fraigneau, On combining linear stochastic estimation and proper orthogonal decomposition for flow reconstruction, *Exp. Fluids* **59**, 58 (2018).
- [24] P. A. Chang III, U. Piomelli, and W. Blake, Relationship between wall pressure and velocity-field sources, *Phys. Fluids* **11**, 3434 (1999).
- [25] M. Ferreira and B. Ganapathisubramani, Scale interactions in velocity and pressure within a turbulent boundary layer developing over a staggered-cube array, *J. Fluid Mech.* **910**, A48 (2021).

- [26] B. Podvin, S. Pellerin, Y. Fraigneau, G. Bonnavion, and O. Cadot, Low-order modelling of the wake dynamics of an Ahmed body, *J. Fluid Mech.* **927**, R6 (2021).
- [27] G. Bonnavion and O. Cadot, Unstable wake dynamics of rectangular flat-backed bluff bodies with inclination and ground proximity, *J. Fluid Mech.* **854**, 196 (2018).
- [28] K. Goda, A multistep technique with implicit difference schemes for calculating two- or three-dimensional cavity flows, *J. Comput. Phys.* **30**, 76 (1979).
- [29] L. Sirovich, Turbulence and the dynamics of coherent structures. Part I: Coherent structures, *Quart. Appl. Math.* **45**, 561 (1987).
- [30] S. Pope, *Turbulent Flows* (Cambridge University Press, Cambridge, England, 2000).
- [31] P. Holmes, J. Lumley, and G. Berkooz, *Turbulence, Coherent Structures, Dynamical Systems and Symmetry* (Cambridge University Press, Cambridge, England, 1996).
- [32] P. Moin and R. Moser, Characteristic-eddy decomposition of turbulence in a channel, *J. Fluid Mech.* **200**, 471 (1989).
- [33] S. Muralidhar, B. Podvin, L. Mathelin, and Y. Fraigneau, Spatio-temporal proper orthogonal decomposition of turbulent channel flow, *J. Fluid Mech.* **864**, 614 (2019).
- [34] L. Soucasse, B. Podvin, P. Rivière, and A. Soufiani, Proper orthogonal decomposition analysis and modelling of large-scale flow reorientations in a cubic Rayleigh-Bénard cell, *J. Fluid Mech.* **881**, 23 (2019).
- [35] B. Podvin, S. Pellerin, Y. Fraigneau, A. Evrard, and O. Cadot, Proper orthogonal decomposition analysis and modelling of the wake deviation behind a squareback Ahmed body, *Phys. Rev. Fluids* **5**, 064612 (2020).
- [36] J. Lumley, The structure of inhomogeneous turbulent flows, in *Atmospheric Turbulence and Radio Wave Propagation*, edited by A. Iaglom and V. Tatarski (Nauka, Moscow, 1967), pp. 221–227.